Journal of Biomedical Optics

SPIEDigitalLibrary.org/jbo

In vivo photoacoustic lifetime imaging of tumor hypoxia in small animals

Qi Shao
Ekaterina Morgounova
Chunlan Jiang
Jeunghwan Choi
John Bischof
Shai Ashkenazi

SPIE

In vivo photoacoustic lifetime imaging of tumor hypoxia in small animals

Qi Shao,[a] Ekaterina Morgounova,[a] Chunlan Jiang,[b] Jeunghwan Choi,[b] John Bischof,[a,b] and Shai Ashkenazi[a]
[a]University of Minnesota, Department of Biomedical Engineering, 7-105 Hasselmo Hall, 312 Church Street SE, Minneapolis, Minnesota 55455
[b]University of Minnesota, Department of Mechanical Engineering, 111 Church Street SE, Minneapolis, Minnesota 55455

Abstract. Tumor hypoxia is an important factor in assessment of both cancer progression and cancer treatment efficacy. This has driven a substantial effort toward development of imaging modalities that can directly measure oxygen distribution and therefore hypoxia in tissue. Although several approaches to measure hypoxia exist, direct measurement of tissue oxygen through an imaging approach is still an unmet need. To address this, we present a new approach based on *in vivo* application of photoacoustic lifetime imaging (PALI) to map the distribution of oxygen partial pressure (pO_2) in tissue. This method utilizes methylene blue, a dye widely used in clinical applications, as an oxygen-sensitive imaging agent. PALI measurement of oxygen relies upon pO_2-dependent excitation lifetime of the dye. A multimodal imaging system was designed and built to achieve ultrasound (US), photoacoustic, and PALI imaging within the same system. Nude mice bearing LNCaP xenograft hindlimb tumors were used as the target tissue. Hypoxic regions were identified within the tumor in a combined US/PALI image. Finally, the statistical distributions of pO_2 in tumor, normal, and control tissues were compared with measurements by a needle-mounted oxygen probe. A statistically significant drop in mean pO_2 was consistently detected by both methods in tumors. [DOI: 10.1117/1.JBO.18.7.076019]

Keywords: tumor hypoxia; methylene blue; tissue oxygen; pO_2; photoacoustic lifetime imaging.

Paper 12684RRRR received Oct. 16, 2012; revised manuscript received May 20, 2013; accepted for publication Jun. 21, 2013; published online Jul. 22, 2013.

1 Introduction

Regions of hypoxia are commonly found in solid tumors. Hypoxia is caused by abnormally low oxygen transport[1] and an imbalance in the supply and consumption of oxygen.[2] Furthermore, tumor hypoxia is strongly linked to a low treatment efficacy in chemotherapy and radiotherapy for several types of human tumors.[3,4] Hypoxia is also correlated with aggressive tumor phenotype and poor prognosis.[5] Some studies suggest that tumor hypoxia does not depend on tumor size, grade, or extent of necrosis.[6] It has also been shown that tumor oxygenation is not correlated with oxygen saturation of hemoglobin in blood (sO_2).[7] Monitoring oxygen partial pressure (pO_2) in tumors has profound implications for the planning of effective therapeutic strategies[8,9] and for assessing methods of modulating tissue oxygen to enhance the efficacy of cancer treatments.

The chemical and physical properties of oxygen enable a wide variety of methods for measuring pO_2 *in vivo* by both local and regional methods. Clinically, the gold standard is based on the local computerized polarographic needle electrode method.[10] However, these systems are invasive and not capable of mapping (imaging) the oxygen content in tissue. Characterizing the heterogeneity of oxygen distribution over the region of interest is valuable in investigating the underlying pathophysiology as well as for making clinical treatments more effective.[11]

This has led to the development of oxygen content imaging methods that can be categorized into three groups: optical, nuclear, and magnetic resonance based. While all these methods provide information about oxygen, each of them has significant limitations. Optical methods including near-infrared spectroscopy[12] and phosphorescence imaging[13] suffer from low penetration depth due to the strong optical scattering in tissue. Nuclear methods use various hypoxia-related probes for positron emission tomography[14] and single-photon emission computed tomography.[15] These radiolabeled compounds indicate activity of cell metabolism, which is not directly related to oxygen content in tissue. Moreover, interpreting the images for identification of hypoxic regions is highly susceptible to time delay between injection of contrast agent and image acquisition.[16] Magnetic resonance based methods include blood oxygen level–dependent magnetic resonance imaging (BOLD-MRI) (Ref. 17), ^{19}F MRI (Ref. 18), electron paramagnetic resonance imaging,[19] and proton–electron double resonance imaging.[20] BOLD-MRI assesses the hemoglobin oxygen saturation and thus can only serve as an indirect measure of tissue oxygenation. Moreover, all MRI methods have a long scanning time and therefore cannot generate real-time images. Other disadvantages include their high cost and incompatibility with implants and pacemakers. Real-time oxygen imaging is particularly beneficial in photodynamic therapy (PDT) where tissue oxygenation changes significantly during the course of treatment and can serve as a critical factor for understanding the posttreatment metabolic pathway of the tumor.[21] Because of the aforementioned inherent limitations in optical, nuclear, and MRI-based methods, these modalities are not commonly implemented in a clinical setting. This indicates a strong clinical need for a new oxygen imaging modality.

Address all correspondence to: Qi Shao, University of Minnesota, Department of Biomedical Engineering, 7-105 Hasselmo Hall, 312 Church Street SE, Minneapolis, Minnesota 55455. Tel: 612-625-1833; Fax: 612-626-6583; E-mail: shaox070@umn.edu

0091-3286/2013/$25.00 © 2013 SPIE

In previous work, we have demonstrated the capability of the photoacoustic lifetime imaging (PALI) technique for measuring pO_2 in a phantom.[22] Here, we report our first study in extending this method to image pO_2 distribution *in vivo*. PALI has several distinctive features that make it a promising alternative to current clinical pO_2 imaging methods. It relies on local measurement of triplet state lifetime of a chromophore. The lifetime is highly dependent on pO_2 for chromophores having a sufficiently stable triplet state. This contrast mechanism is similar to those of pO_2 imaging methods based on phosphorescence lifetime.[23] The readout penetration depth and resolution, however, are greatly improved in PALI because the excitation lifetime is measured by photoacoustic imaging (PAI), a technique that circumvents the difficulty posed by strong optical scattering in tissue. Specifically, PAI relies on detection and imaging of acoustic signals generated by light absorption of short laser pulses. Its resolution is determined by the ultrasound (US) transducer that is used for photoacoustic (PA) signal detection and therefore resembles that of US imaging.[24,25] Penetration depth of PAI depends on diffused light penetration in tissue and can reach up to 5 cm.[26,27]

PALI utilizes two pulsed laser sources, one for exciting the chromophore and the other for PA probing of the excited state. The first laser pulse pumps the dye to an excited state. The dynamics of relaxation back to the ground state results in transient optical absorption. This transience can be probed by a second pulsed laser that generates PA waves. The amplitudes of these waves depend linearly on optical absorption in the sample. Because the absorption is time dependent, the amplitudes of the waves change with the time delay between the two pulses. Therefore, by altering this time delay, the decay of the excited state population can be measured and the excited state lifetime can be extracted. The PA signals are detected and then processed to reconstruct a PA image at each pump–probe time delay. The sequence of images is then used to track the decay profile of the excited state independently at each pixel position in the field of view. PALI thus provides an image showing the distribution of the excited state lifetime.

Combining PALI with tissue staining by oxygen-sensitive dye yields a method for tissue oxygen imaging. The oxygen sensitivity of these dyes is based on dynamic quenching of the excited state by collisions with oxygen molecules. High oxygen sensitivity requires that the rate of collisions be higher than the relaxation rate of the excited state. For this reason, long-lifetime dyes are preferred for oxygen sensing. Particularly, useful dyes exhibit efficient intersystem crossing to a metastable triplet state. In this case, the lifetime is typically in the microsecond or even millisecond range.

In this work, we chose to use methylene blue (MB) as an oxygen-sensitive dye. MB is a water-soluble dye that is widely used in clinical diagnostic and therapeutic applications.[28–30] This is due to its low cytotoxicity and efficient clearance from the body via bile, feces, and urine.[31,32] In addition, the lifetime of MB is an intrinsic property and does not depend on its concentration (79.5 μs in oxygen-depleted solution[33]). MB is relatively stable in stained tissue for up to several hours. After this period, transport via blood circulation and lymphatic clearing takes place as well as the reduction of MB to its nonabsorbing leuco form. Because image acquisition time is typically <3 min, this time window of relatively stable dye concentration in the target tissue is long enough to warrant its application in PALI oxygen imaging.

In vivo application of the lifetime-based PA technique has previously been reported by Ray et al.[34] They used G2, a dendrimer-based oxygen-sensitive dye,[35] to measure pO_2 in a single point in the main artery of a rat tail. Their measurements were confined to the blood volume because the G2 dye does not penetrate vessel walls due to its relatively large molecular size.[36,37] In the work presented here, we were able to measure pO_2 in the solid tissue because MB is a small molecule that rapidly stains tissue by diffusion. In order to map the distribution of pO_2 in the solid tissue, a full two-dimensional imaging technique has been implemented.

2 Materials and Methods

2.1 *Multimodal Imaging System*

The schematic of the multimodal system is shown in Fig. 1. The system allowed for three modes of operation: pulse-echo US imaging, PAI, and PALI. The pump laser was a pulsed Nd:YAG laser (Surelite I, Continuum), equipped with a third harmonics generation module, emitting short pulses (5 ns) at 355 nm. An optical parametric oscillator (OPO, MagicPRISM, OPOTEK, Carlsbad, CA) was used in conjunction with the laser to generate a wavelength of 650 nm to match the peak absorption of MB in its ground state. A frequency-doubled Nd:YAG pulsed laser (Brilliant, Quantel, Bozeman, MT, 532 nm, 5 ns) commercially integrated with a second OPO unit served as the probe laser. The integrated laser system (Rainbow, OPOTEK) provided a tuning range from 680 to 960 nm. The output wavelength of this laser system was tuned to 810 nm to match the excited state triplet–triplet peak absorption of MB. The pulse energies at 650 and 810 nm were measured to be 8 and 10 mJ, respectively. A set of prisms was used to align the two beams such that they overlapped at the surface of the imaging object. The light intensities of the two beams were approximately 8 and 13 mJ/cm^2, which are below the ANSI limit.[38]

Both the lasers were externally triggered by an field-programmable gate array (FPGA) module (Saxo FPGA board, KNJN, California) at a 10 Hz repetition rate. The time delay between the pump and probe pulses was controlled by a PC via a parallel port connection to the FPGA module. The module

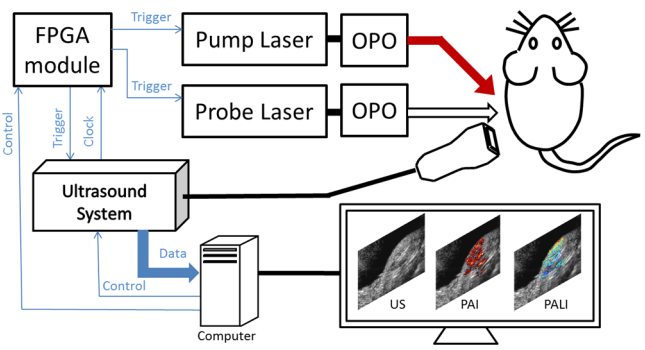

Fig. 1 Schematic of *in vivo* multimodal imaging system. The system was capable of generating ultrasound (US), photoacoustic imaging (PAI), and photoacoustic lifetime imaging (PALI) images using the same hardware. The animal was illuminated by two laser systems triggered by an FPGA module. Both pulse-echo US and PA signals were acquired by a conventional phased-array US transducer and then amplified, digitized, and stored in the US system. Data were transferred to a PC for image processing and display.

also triggered the signal acquisition of a 64-channel US system (OPEN system, Lecoeur Electronique, Chuelles, France). The US system was connected to a 64-element US phased-array transducer (P7-4, ATL). This transducer has 64 elements arranged in a linear array configuration with interelement spacing of 0.18 mm. The center frequency of the transducer is 5 MHz and its bandwidth is 3 MHz. The same transducer was used as a transmitter–receiver in pulse-echo US imaging mode and as a receiver-only in PAI and PALI. All the 64 channels were digitized simultaneously at 12-bit resolution. The amplification gain of each channel can be programmed from 0 to 79.9 dB. The data were stored in an internal buffer and then transferred to a PC for image reconstruction and processing. The 80-MHz internal clock of the US system was utilized as a common time-base for all other clocks and triggering signals in the multimodal imaging system, thereby ensuring minimal jitter between laser pulses and PA signal acquisition.

2.2 *US Imaging*

In US imaging mode, the lasers were turned off, and the US system triggering was set to internal. The US images were obtained by the synthetic transmit aperture method.[39,40] At each step, only one channel of the phased array emitted an US pulse, and the reflected backscattering signals were simultaneously recorded on all 64 channels. This step was repeated until the echo signals from every emitting channel were acquired. The signal acquisition time for a complete scan was <100 ms. This method generates a data set from which signals corresponding to any pair of emitting and receiving elements can be extracted. For each emitting element, an amplitude image was reconstructed by the delay-and-sum method,[41] followed by Hilbert transformation along the axial direction for conversion to a complex, analytical signal. Finally, all complex amplitude images were summed, and the absolute values were presented using dB scales.

2.3 *PAI and PALI*

When working in PAI and PALI modes, both lasers were turned on, and the US system was then set to external triggering mode with the US pulse generator turned off to reduce electronic noise. The PA signal acquired by the US array was averaged over 100 measurements to compensate for the fluctuations in the OPO output energy. A filtered backprojection algorithm was applied to reconstruct the PA images.[42] The PA signal was filtered by a zero phase-shift finite impulse response filter with bandwidth of 3 to 7 MHz and then processed through a coherent summation procedure to generate the PA amplitude at each pixel in the field of view. Envelope detection was then applied by taking the absolute value of the Hilbert transform of the PA amplitudes along lines in the depth direction. The final step was required for generating a unipolar PA image.

A series of PA signals was obtained with pump–probe delays (τ) of 0.25 μs, 0.5 μs, 1 μs, 2 μs, 4 μs, 8 μs, and 100 ms. The delay was accomplished by changing the time of the pump with respect to the triggering signal to US system. At each delay, PA signals were recorded with the probe beam both on (synchronized with start of US signal acquisition) and off. Taking into account the 10-Hz repetition rate and the time for data transfer, the total imaging acquisition time was ~150 s. This includes averaging of 100 samples for each PA signal. In order to extract the transient PA signal, the following steps were applied. First, the PA signal corresponding to the 810-nm laser (S_{810}) was calculated by subtracting the PA signal generated by the 650-nm laser only (S_{650}) from the PA signals generated with both lasers (650 and 810 nm) emitting ($S_{810+650}$) at a specific pump–probe time delay (τ_0), as described by Eq. (1).

$$S_{810,\tau=\tau_0} = S_{650+810,\tau=\tau_0} - S_{650,\tau=\tau_0}. \tag{1}$$

The S_{810} signal had two independent components, a background absorption signal due to light absorption in tissue (mostly in hemoglobin) ($S_{810,\text{background}}$) and a transient absorption signal of MB at τ_0 ($S_{810,\text{transient},\tau=\tau_0}$). The two components were separated using a background suppression method described by Huang et al.[43] in more detail below. The background absorption is independent of the pump–probe time delay. Therefore, the background PA signal was obtained by separating the two individual PA responses (650 and 810 nm) at a long τ (100 ms), a value that is much longer than the normal range of lifetime of MB (<100 μs). The transient PA signal was then obtained by subtracting the background PA signal at 810 nm from the total PA signal at 810 nm.

$$S_{810,\text{background}} = S_{650+810,\tau=100\text{ ms}} - S_{650,\tau=100\text{ ms}}, \tag{2}$$

$$S_{810,\text{transient},\tau=\tau_0} = S_{810,\tau=\tau_0} - S_{810,\text{background}}. \tag{3}$$

A sequence of PA amplitude images of the transient absorption was then reconstructed from the transient PA signal $S_{810,\text{transient},\tau=\tau_0}$. Each image in the sequence corresponds to a different time delay. The following set of time delays was used: 0.25, 0.5, 1, 2, 4, and 8 μs. For each pixel, the lifetime (T) and the transient PA amplitude (A_0) were computed by fitting the amplitude (A) to an exponential decay function of the pump–probe delay τ:

$$A = A_0 e^{-\frac{1}{T}\tau}. \tag{4}$$

Additionally, the coefficient of determination, R^2, was computed at each pixel to reflect the goodness of fit. The amplitude threshold was set to be a quarter of the global maximum amplitude of the PA image. An amplitude above threshold and an R^2 value >0.8 were used as selection criteria to ensure the validity of lifetime estimates. Only pixels that met both criteria were converted to pO_2 values and displayed in a color scale. The Stern–Volmer relationship [Eq. (5)] describing the lifetime as a function of pO_2[44] was used to convert lifetime to pO_2:

$$\frac{T^0}{T} = 1 + k_Q T^0 \text{pO}_2, \tag{5}$$

where T^0 is the lifetime at $pO_2 = 0$, and k_Q is the quenching rate constant. For MB, $T^0 = 79.5$ μs, and $k_Q = 0.0036$ μs^{-1} $mmHg^{-1}$.[33]

2.4 *Phantom Imaging*

To demonstrate the capability of multimodal imaging, we tested the imaging system using a phantom consisting of two tubes. The experimental setup is shown in Fig. 2(a) and 2(b). Two plastic tubes (inner diameter 0.7 mm and outer diameter 2.4 mm) containing MB aqueous solution at different pO_2 values were placed perpendicular to the scanning plane. The solution in each tube was in closedflow circulation with an oxygenation

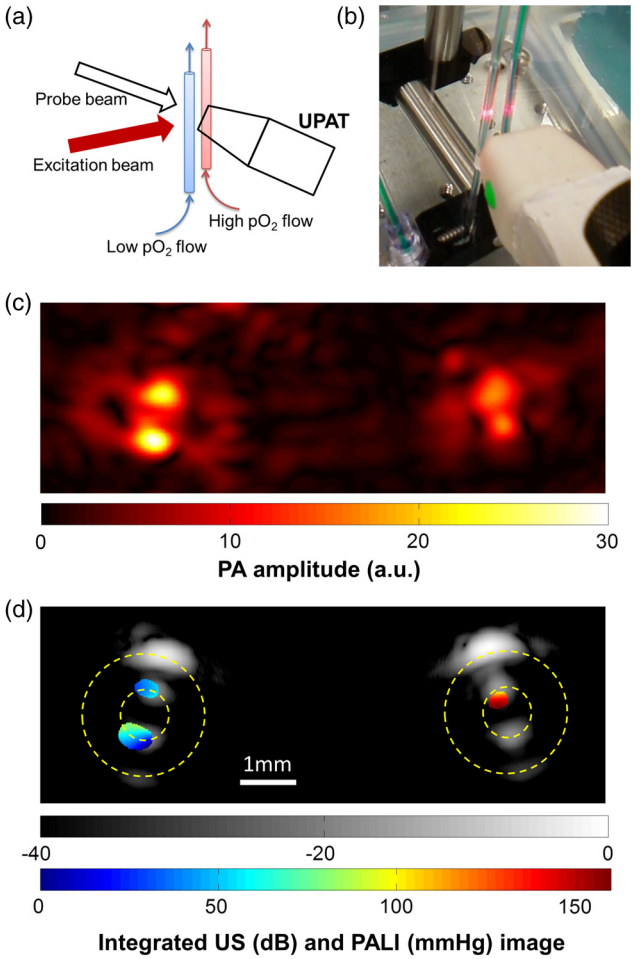

Fig. 2 Experimental setup and multimodal imaging results of a two-tube phantom experiment. (a) The phantom consists of two plastic tubes containing methylene blue (MB) aqueous solution at high pO_2 (150 mmHg, right) and low pO_2 (50 mmHg, left). Both tubes were illuminated by the excitation beam (650-nm laser) and probe beam (810-nm laser). (b) Photo of the phantom and the US transducer. UPAT, ultrasound phased-array transducer. (c) Transient PA image of the two tubes by the 810-nm laser at a pump–probe delay of 0.5 μs displayed in a linear scale. The two clusters of PA signals represent the location of the wall–dye interface in the two tubes. The phantom was illuminated by two lasers from the left, resulting in higher PA amplitude in the left tube. (d) PALI image (color) superposed on US (gray scale) image. Inner and outer walls of both tubes are indicated by dashed lines.

cell, in which the pO_2 level was controlled by gas bubbling. One cell was bubbled by air so that the pO_2 of the solution was air-equilibrated, and the other one was bubbled by pure nitrogen. The US transducer was placed near the tubes, with both lasers illuminating the tubes from the side [left side of Fig. 2(a)]. Both PA and US signals were recorded without moving the tubes and transducer. PA images at a series of time delays were reconstructed, and the lifetime was extracted and converted to pO_2 for display.

2.5 *Animal Preparation*

Tumor-bearing nude mice were used as a cancer model in this study. Tumors were induced by injecting LNCaP cells into the hindlimbs. The LNCaP cell line was derived from human prostate adenocarcinoma and has been commonly used in cancer research.[45–47] Specifically, 1×10^6 cells suspended in 0.1 mL Matrigel matrix (50% Matrigel and 50% LNCaP growth medium) were subcutaneously injected into the hindlimb of each 24-g nude mouse. Tumors grown for 3 to 5 weeks with a diameter of 5 to 10 mm were considered appropriate for further experiments.

Methylene blue (MB hydrate, Fluka, Sigma-Aldrich, St. Louis, MO) was dissolved in physiological saline (DPBS 1×, Mediatech, Manassas, VA) to a concentration of 5 mM. After the animal was anesthetized by ketamine (100 mg/kg) and xylazine (10 mg/kg), the MB solution was injected into the hindlimb. The amount of MB injection was 0.2 to 0.6 mL at each spot (5 to 10 mm between injection spots, total injection volume was limited to 1 mL for a given hindlimb). Data acquisition was initiated after 10 to 15 min to allow the dye to sufficiently diffuse in the tissue. All animal procedures and care were performed according to protocols approved by the University of Minnesota Institutional Animal Care and Use Committee in accordance with federally approved guidelines.

2.6 *In Vivo Oxygen Imaging and Measurement*

The animals were divided into two groups: mice with hindlimb tumor (group A, $n_A = 8$) and control non–tumor-bearing mice (group B, $n_B = 10$). Two animals from each group were randomly chosen for imaging, whereas the rest were used for direct measurements using an oxygen probe for comparison. In group A, both the PALI and oxygen probe were applied to quantify the pO_2 of the tumor and normal tissue at the hindlimbs. In group B, pO_2 of the non–tumor-bearing hindlimb of control mice were measured by both methods. The pO_2 values in PALI were obtained from individual pixel values within regions of interest in the images, whereas the pO_2 values by the oxygen probe were directly recorded. The statistics of pO_2 values obtained by PALI and the probe with three types of tissues (tumor tissue, normal tissue, and control mice) were compared.

The animal chosen for imaging was transferred to the imaging platform as shown in Fig. 3. The imaging platform included an animal holder in order to keep the hindlimb of the animal submerged in water and the head above the surface for normal breathing. The transducer and platform were fixed by mechanical arms so that the relative position of the animal and US transducer did not change throughout the experiment. The water temperature was kept at 35 °C ± 0.5 °C by a digital heating system (T3-150, Transworld Aquatic Enterprises, Inglewood, CA). The US images were generated to provide the anatomical structure of the hindlimb. PA images at each pump–probe delay were obtained and then processed to yield the PALI image. After the imaging procedures, the animal was euthanized.

To perform direct oxygen measurements, the animal was first anesthetized and transferred to a heater pad. The pO_2 of the hindlimb was then assessed by a commercial single-point oxygen probe. The device consists of a retractable needle-type oxygen sensor (sensor tip diameter 50 μm, surrounded by a 40-mm-long and 0.8-mm-wide syringe needle, OXR50, Pyroscience, Aachen, Germany) and optical oxygen meter (Firesting O_2, Pyroscience). The Firesting O_2 system is a PC-controlled fiber-optic oxygen meter that measures pO_2 by quantifying the oxygen-dependent phosphorescence of a dye-stained polymer membrane located at the tip of the optical fiber. The oxygen sensor was inserted into tissue with the needle. By pulling out the probe in a step-wise manner, pO_2 values along the needle path at different depths were recorded. Typically, three needle penetrations were made in one hindlimb and two to four stable

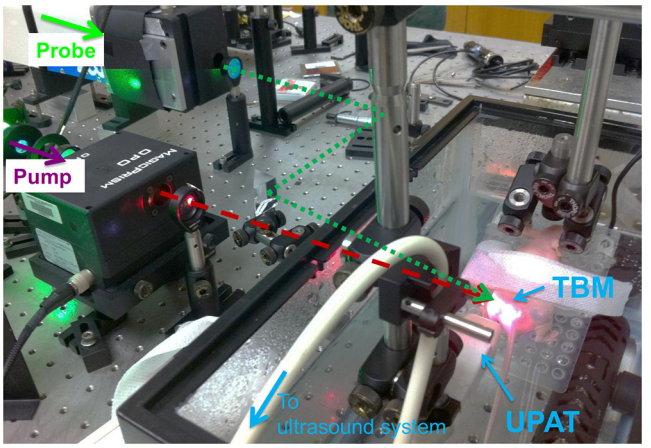

Fig. 3 *In vivo* imaging platform for small animals. The nude mouse was fixed within a water tank with its head above the water level. Two laser beams overlapped on the tumor-bearing hindlimb, while the US transducer was positioned next to the illuminated spot and aligned for multimodal imaging. TBM, tumor-bearing mouse; UPAT, ultrasound phased-array transducer. Red dashed line, the 650-nm laser beam; green dotted line, the 810-nm laser beam.

pO_2 readings were recorded for each penetration. The animal was euthanized after the measurements.

3 Results

3.1 *Phantom Imaging*

An example of multimodal imaging results of a phantom is given in Fig. 2(c) and 2(d). Figure 2(c) shows the PA image of the phantom. Figure 2(d) shows the superposition of the PALI image onto the US image. Both the PA and US images correctly reflect the structure of the phantom, with the PA image showing the optical absorption of the contents inside the tubes and the US image indicating the inner and outer walls. The different levels of pO_2 in the two tubes are shown in the PALI image. The pO_2 within the left and right tubes were set to 50 and 150 mmHg, respectively. The PALI image clearly shows the levels in the range of 40 to 60 mmHg and 130 to 160 mmHg for the left and right tubes, respectively.

3.2 *In Vivo Imaging*

The setup for the *in vivo* measurements is shown in Fig. 3. PA and PALI images were superposed onto the US image. As can be seen from Fig. 3, the laser beams illuminated only a portion of the hindlimb due to the limited power of the lasers. Therefore, both PA and PALI images covered less area than the US image [Fig. 4(a)]. The PA image shows the amplitude distribution resulting from the background absorption [Fig. 4(b)] and MB's transient absorption [Fig. 4(c)]. The transient PA amplitudes associated with two pixels, along with their exponential decay determined by curvefitting, are shown in Fig. 4(e). The two pixels correspond to points with high and low pO_2. The hypoxic region imaged by PALI [Fig. 4(d)] is consistent with the site of the tumor imaged by US. We have also applied the same technique to the control mice without tumor. The PALI images indicate inhomogeneous tissue oxygenation within the normal muscle tissue, and the pO_2 values were within the normal physiological range.

3.3 *Correlative In Vivo Measurement*

We have performed correlative direct measurements using the oxygen needle sensor in tumor-bearing mice and control mice. The total number of valid pO_2 readings for tumor tissue, normal tissue of tumor-bearing mice, and control mice was 38, 39, and 121, respectively. The three groups of measurements were then compared with the pO_2 values extracted from PALI images. The frequency distributions of the pO_2 values are displayed in a histogram shown in Fig. 5(a). The three regions for statistical analysis of pO_2 distribution via PALI are labeled in Fig. 5(b) and 5(c). We performed two-sample *t*-tests. The results show a statistically significant difference in pO_2 distribution between tumors and other tissues, with p values <0.05 by both PALI and the needle probe. Both PALI and direct oxygen measurements confirmed that the tissue oxygen level in the tumors is significantly lower (~20mmHg) than that in normal tissue and control mice.

4 Discussion

Tissue pO_2 is a key regulator of physiological function, and changes in tissue oxygenation play a critical role in the pathophysiology of a wide range of diseases. In cancer, particularly, low pO_2 in tumors indicates poor prognosis and low efficacy of radiotherapy and chemotherapy. Imaging of pO_2 can significantly improve the quality of diagnosis and treatment planning for cancer patients. Nevertheless, current imaging modalities fail to provide a suitable clinical solution.

In this work, we have demonstrated the *in vivo* application of PALI for tissue oxygen imaging in small animals. PALI is a novel and alternative method for *in vivo* oxygen imaging with the advantages of rapid image acquisition, involving nonionizing laser radiation and using a nonradioactive optical contrast agent. In this work, we used MB, a dye that has been widely used in therapeutic and diagnostic applications. The imaging results confirm the existence of hypoxic area caused by the solid tumor. The statistical distribution of pO_2 was compared to direct measurements by an optical needle sensor system. An overall shift toward higher pO_2 values in PALI compared to direct measurements was found. This may have resulted from the higher body temperature during PALI imaging (water temperature of 35°C) versus needle sensor measurements (room temperature of 22°C), which might affect blood circulation and tissue oxygenation.

To achieve these measurements, a multimodal (US imaging, PAI, PALI) imaging system has been developed. All three imaging modes share the same US transducer, thereby eliminating the need for image coregistration of anatomical and functional informations. The system employs a commercial 64-element phased-array US transducer. It is optimally designed for clinical US imaging in applications such as echocardiography where limited aperture is required.

The limitations imposed by the limited bandwidth and aperture size compromise accurate reconstruction of large-scale structures. The problem of implementing PAI using US imaging arrays has been investigated by several groups.[48–50] These studies show that PA images can still adequately represent tissue structure and morphology by relying on differences in small-scale structure of different tissue types and on the high visibility of interfaces causing abrupt gradients in optical absorption.

The phantom imaging results demonstrate that the system was able to achieve pO_2 distribution of submillimeter structures.

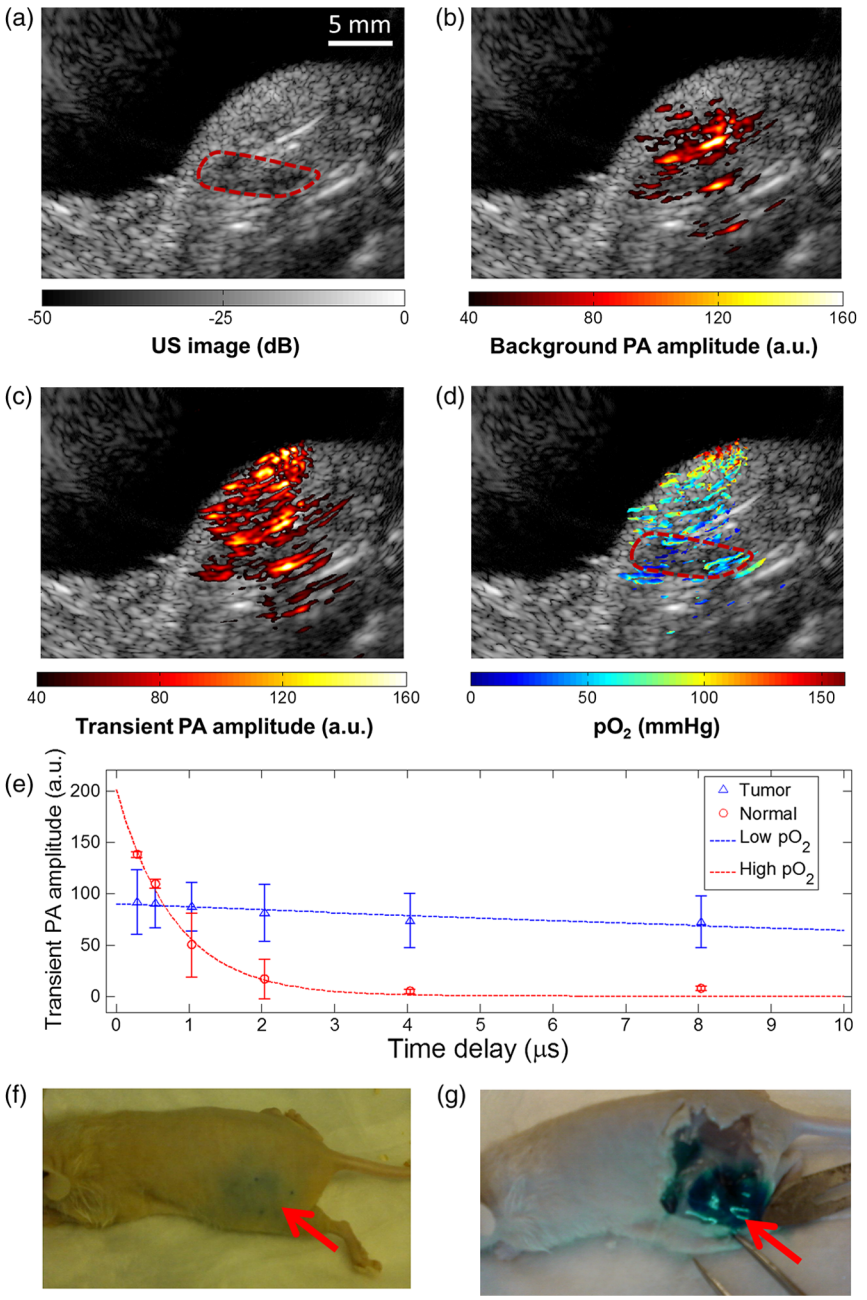

Fig. 4 Multimodal imaging of the tumor-bearing mice. (a) US image of the left tumor-bearing hindlimb of a mouse. The area of the tumor is enclosed by a red dashed line. (b) PAI representing the amplitude of background absorption at 810 nm. Amplitude is displayed in linear scale. (c) PAI of the transient absorption of MB with an 810-nm laser at a pump–probe delay of 0.25 μs. (d) PALI of pO_2 in color scale superimposed on US image. (e) Transient PA amplitudes of two representative pixels within the tumor and in normal control tissue, respectively. The triangles and circles are the averaged transient PA amplitudes of tumor and normal control tissue, respectively. The error bars represent the standard deviation of 100 recordings. Both the sets of data were fitted with an exponential curve as shown by the dashed line. (f) Animal after imaging procedure. An arrow indicates the MB stained imaging region. (g) Open-skin view of the tumor site. Note that the tissue was still stained with MB after the imaging process, thereby confirming stable MB staining of the tissue for a period of >1 h. The red arrow indicates the site of the tumor.

Based on the resulting *in vivo* PALI images, the maximal imaging depth of the system is estimated to be ~12 mm. The imaging depth is expected to be improved by increasing the laser energy density. The images also show lack of continuity in the field of view. The regions of valid PALI data consist of isolated "islands" in the field of view. This is mostly a result of low intensity of the excitation laser pulse resulting in low excitation efficiency. This limitation is primarily due to the finite penetration depth of the excitation light in tissue.

One of the advantages of sensing oxygen via PA lifetime is its robustness to large variations in the concentration of the oxygen-sensitive dye and in the intensity of the light. However, low concentrations of the dye and inadequate fluence rate both contribute to a reduction in signal-to-noise ratio, making oxygen measurement less accurate. An additional source of noise is attributed to the fluctuations in the pulse energy of both the pump and probe laser. A set of criteria has been developed and implemented to validate the oxygen information. These

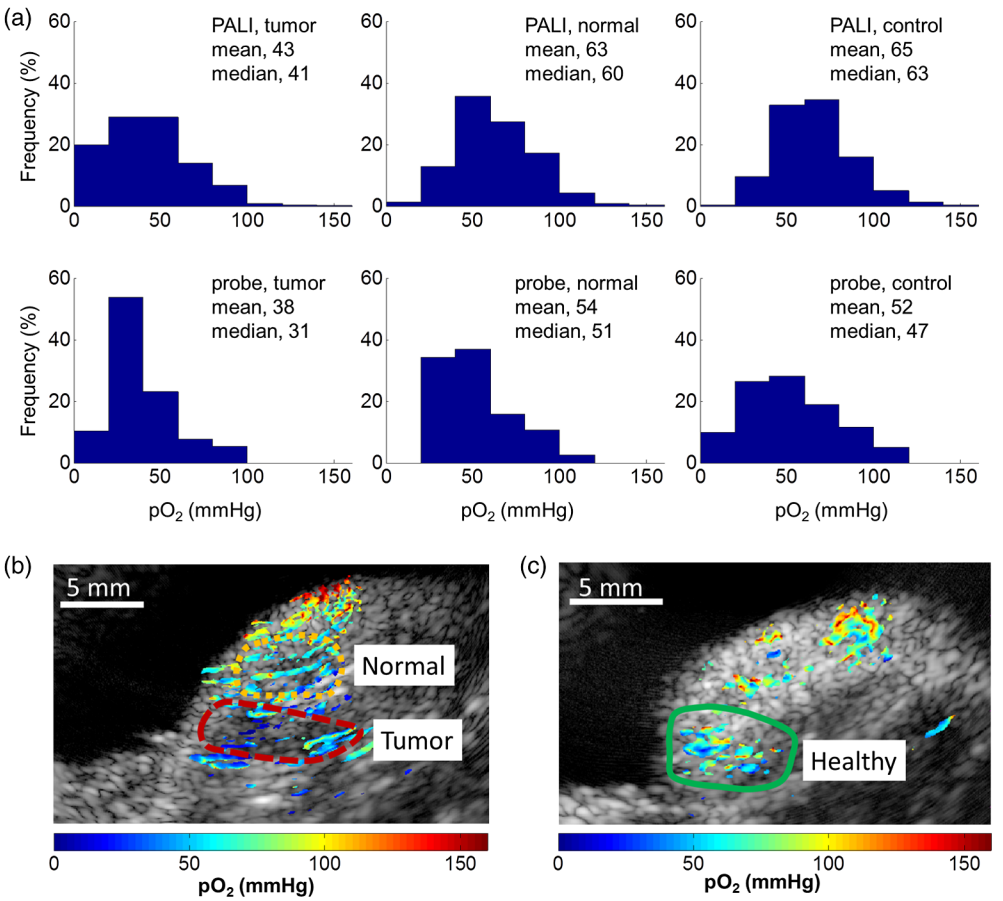

Fig. 5 Histogram of pO_2 in tumor tissue, normal tissue, and control mice. (a) Top row: histogram of pO_2 values extracted from PALI. Bottom row: histogram of pO_2 values measured by the oxygen probe. Data from tumor tissue, normal tissue (adjacent to tumor site), and control tissue (no tumor present) are displayed in left, middle, and right columns, respectively. (b) PALI showing the regions of tumor (red dashed line) and normal (yellow dashed line) sites in a tumor-bearing hindlimb of a mouse. (c) PALI showing the control tissue of a tumor-free hindlimb. The image does not show a substantial area of low pO_2 as compared to Fig. 4(d).

criteria include a high PA amplitude level and a high R^2 value for exponential fit used for evaluating lifetime.

The results presented indicate that PALI can be used for mapping tissue oxygen *in vivo*. Furthermore, the work demonstrates the technical capability of multimodality imaging (US, PAI, and PALI) and its usefulness in visualizing functional imaging data. The technique is very attractive for a range of clinical applications in which tissue oxygen mapping would improve therapy decision making and treatment planning. Examples include cancer treatments (radiotherapy and PDT) and treatments of diabetes-related ulcers. A more comprehensive validation study of PALI is still required before its implementation in clinical applications could be established. In addition, other methods of light delivery, such as the use of minimallyinvasive, tissue-penetrating fiber diffusers, should be explored in order to extend the applicability of PALI into an even broader range of clinical applications.

Acknowledgments

The authors would like to thank Mr. Clay Sheaff for his close reading of the manuscript and valuable comments. This work was sponsored by National Institutes of Health grant R21 CA135027.

References

1. M. E. Hardee et al., "Novel imaging provides new insights into mechanisms of oxygen transport in tumors," *Curr. Mol. Med.* **9**(4), 435–441 (2009).
2. O. Thews et al., "Can tumor oxygenation be improved by reducing cellular oxygen consumption," *Adv. Exp. Med. Biol.* **471**, 525–532 (1999).
3. P. Okunieff et al., "Oxygen-tension distributions are sufficient to explain the local response of human breast-tumors treated with radiation alone," *Int. J. Radiat. Oncol. Biol. Phys.* **26**(4), 631–636 (1993).
4. M. Hockel et al., "Intratumoral pO_2 predicts survival in advanced cancer of the uterine cervix," *Radiother. Oncol.* **26**(1), 45–50 (1993).
5. A. Bratasz et al., "In vivo imaging of changes in tumor oxygenation during growth and after treatment," *Magn. Reson. Med.* **57**(5), 950–959 (2007).
6. J. M. Brown, "A target for selective cancer therapy—Eighteenth Bruce F. Cain Memorial Award Lecture," *Cancer Res.* **59**(23), 5863–5870 (1999).
7. J. G. Rajendran and K. A. Krohn, "Imaging hypoxia and angiogenesis in tumors," *Radiol. Clin. North Am.* **43**(1), 169–187 (2005).
8. C. Menon and D. L. Fraker, "Tumor oxygenation status as a prognostic marker," *Cancer Lett.* **221**(2), 225–235 (2005).
9. S. M. Evans and C. J. Koch, "Prognostic significance of tumor oxygenation in humans," *Cancer Lett.* **195**(1), 1–16 (2003).
10. P. Vaupel et al., "Oxygenation of human tumors: evaluation of tissue oxygen distribution in breast cancers by computerized O_2 tension measurements," *Cancer Res.* **51**(12), 3316–3322 (1991).

11. D. S. Vikram, J. L. Zweier, and P. Kuppusamy, "Methods for noninvasive imaging of tissue hypoxia," *Antioxid. Redox Signaling* **9**(10), 1745–1756 (2007).
12. J. C. Hebden et al., "Three-dimensional optical tomography of the premature infant brain," *Phys. Med. Biol.* **47**(23), 4155–4166 (2002).
13. D. F. Wilson et al., "Oxygen distribution and vascular injury in the mouse eye measured by phosphorescence-lifetime imaging," *Appl. Opt.* **44**(25), 5239–5248 (2005).
14. B. J. Krause et al., "PET and PET/CT studies of tumor tissue oxygenation," *Quart. J. Nucl. Med. Mol. Imag.* **50**(1), 28–43 (2006).
15. R. C. Urtasun et al., "Measurement of hypoxia in human tumours by non-invasive SPECT imaging of iodoazomycin arabinoside," *Br. J. Cancer Suppl.* **27**, S209–S212 (1996).
16. J. L. Tatum et al., "Hypoxia: importance in tumor biology, noninvasive measurement by imaging, and value of its measurement in the management of cancer therapy," *Int. J. Radiat. Biol.* **82**(10), 699–757 (2006).
17. M. Stubbs, "Application of magnetic resonance techniques for imaging tumour physiology," *Acta Oncol.* **38**(7), 845–853 (1999).
18. J. X. Yu et al., "F-19: a versatile reporter for non-invasive physiology and pharmacology using magnetic resonance," *Curr. Med. Chem.* **12**(7), 819–848 (2005).
19. M. Elas et al., "Quantitative tumor oxymetric images from 4D electron paramagnetic resonance imaging (EPRI): methodology and comparison with blood oxygen level-dependent (BOLD) MRI," *Magn. Reson. Med.* **49**(4), 682–691 (2003).
20. T. Liebgott et al., "Proton electron double resonance imaging (PEDRI) of the isolated beating rat heart," *Magn. Reson. Med.* **50**(2), 391–399 (2003).
21. Q. Chen, H. Chen, and F. W. Hetzel, "Tumor oxygenation changes post-photodynamic therapy," *Photochem. Photobiol.* **63**(1), 128–131 (1996).
22. S. Ashkenazi, "Photoacoustic lifetime imaging of dissolved oxygen using methylene blue," *J. Biomed. Opt.* **15**(4), 040501 (2010).
23. S. Ashkenazi et al., "Photoacoustic probing of fluorophore excited state lifetime with application to oxygen sensing," *J. Biomed. Opt.* **13**(3), 034023 (2008).
24. A. Buehler et al., "Three-dimensional optoacoustic tomography at video rate," *Opt. Express* **20**(20), 22712–22719 (2012).
25. S. A. Ermilov et al., "Laser optoacoustic imaging system for detection of breast cancer," *J. Biomed. Opt.* **14**(2), 024007 (2009).
26. K. H. Song and L. V. Wang, "Deep reflection-mode photoacoustic imaging of biological tissue," *J. Biomed. Opt.* **12**(6), 060503 (2007).
27. G. Ku and L. V. Wang, "Deeply penetrating photoacoustic tomography in biological tissues enhanced with an optical contrast agent," *Opt. Lett.* **30**(5), 507–509 (2005).
28. K. Orth et al., "Methylene blue mediated photodynamic therapy in experimental colorectal tumors in mice," *J. Photochem. Photobiol. BBiol.* **57**(2–3) (2000).
29. I. Fukui et al., "In vivo staining test with methylene blue for bladder cancer," *J. Urol.* **130**(2), 252–255 (1983).
30. E. M. Tuite and J. M. Kelly, "Photochemical interactions of methylene blue and analogues with DNA and other biological substrates," *J. Photochem. Photobiol. B* **21**(2–3), 103–124 (1993).
31. J. Clifton, II and J. B. Leikin, "Methylene blue," *Am. J. Ther.* **10**(4), 289–291 (2003).
32. G. C. Buehring and H. M. Jensen, "Lack of toxicity of methylene blue chloride to supravitally stained human mammary tissues," *Cancer Res.* **43**(12 Part 1), 6039–6044 (1983).
33. M. Gonzalez-Bejar et al., "Methylene blue encapsulation in Cucurbit 7 uril: laser flash photolysis and near-IR luminescence studies of the Interaction with oxygen," *Langmuir* **25**(18), 10490–10494 (2009).
34. A. Ray et al., "Lifetime-based photoacoustic oxygen sensing in vivo," *J. Biomed. Opt.* **17**(5), 057004 (2012).
35. I. Dunphy, S. A. Vinogradov, and D. F. Wilson, "Oxyphor R2 and G2: phosphors for measuring oxygen by oxygen-dependent quenching of phosphorescence," *Anal. Biochem.* **310**(2), 191–198 (2002).
36. L. S. Ziemer et al., "Oxygen distribution in murine tumors: characterization using oxygen-dependent quenching of phosphorescence," *J. Appl. Physiol.* **98**(4), 1503–1510 (2005).
37. A. Y. Lebedev et al., "Dendritic phosphorescent probes for oxygen imaging in biological systems," *ACS Appl. Mater. Interfaces* **1**(6), 1292–1304 (2009).
38. ANSI Laser Institute of America, "American National Standard for Safe Use of Lasers: ANSI Z136.1-2000," American National Standards Institute, New York (2000).
39. J. A. Jensen et al., "Synthetic aperture ultrasound imaging," *Ultrasonics* **44**, e5–e15 (2006).
40. I. Trots, A. Nowicki, and M. Lewandowski, "Synthetic transmit aperture in ultrasound imaging," *Arch. Acoust.* **34**(4), 685–695 (2009).
41. M. H. Pedersen, K. L. Gammelmark, and J. A. Jensen, "In-vivo evaluation of convex array synthetic aperture imaging," *Ultrasound Med. Biol.* **33**(1), 37–47 (2007).
42. Y. Xu et al., "Reconstructions in limited-view thermoacoustic tomography," *Med. Phys.* **31**(4), 724–733 (2004).
43. S. W. Huang et al., "Differential-absorption photoacoustic imaging," *Opt. Lett.* **34**(16), 2393–2395 (2009).
44. J. M. Vanderkooi and D. F. Wilson, "A new method for measuring oxygen concentration in biological systems," *Adv. Exp. Med. Biol.* **200**, 189–193 (1986).
45. M. M. Shenoi et al., "Nanoparticle preconditioning for enhanced thermal therapies in cancer," *Nanomedicine (Lond)* **6**(3), 545–563 (2011).
46. J. S. Horoszewicz et al., "LNCaP model of human prostatic carcinoma," *Cancer Res.* **43**(4), 1809–1818 (1983).
47. C. A. Pettaway et al., "Selection of highly metastatic variants of different human prostatic carcinomas using orthotopic implantation in nude mice," *Clin. Cancer Res.* **2**(9), 1627–1636 (1996).
48. C. Kim et al., "Deeply penetrating in vivo photoacoustic imaging using a clinical ultrasound array system," *Biomed. Opt. Express* **1**(1), 278–284 (2010).
49. S. A. Ermilov et al., "Development of laser optoacoustic and ultrasonic imaging system for breast cancer utilizing handheld array probes," *Proc. SPIE* **7177**, 717703 (2009).
50. R. G. Kolkman et al., "Real-time in vivo photoacoustic and ultrasound imaging," *J. Biomed. Opt.* **13**(5), 050510 (2008).